

A bosonic perspective on the classical mapping of fermionic quantum dynamics

Jing Sun,^{1, a)} Sudip Sasmal,^{1, b)} and Oriol Vendrell^{1, c)}

Theoretische Chemie, Physikalisch-Chemisches Institut, Universität Heidelberg, Germany.

(Dated: 15 September 2021)

We consider the application of the original Meyer-Miller (MM) Hamiltonian to mapping fermionic quantum dynamics to classical equations of motion. Non-interacting fermionic and bosonic systems share the same one-body density dynamics when evolving from the same initial many-body state. The MM classical mapping is exact for non-interacting bosons, and therefore it yields the exact time-dependent one-body density for non-interacting fermions as well. Starting from this observation, the MM mapping is compared to different mappings specific for fermionic systems, namely the spin mapping (SM) with and without including a Jordan-Wigner transformation, and the Li-Miller mapping (LMM). For non-interacting systems, the inclusion of fermionic anti-symmetry through the Jordan-Wigner transform does not lead to any improvement in the performance of the mappings and instead it worsens the classical description. For an interacting impurity model and for models of excitonic energy transfer, the MM and LMM mappings perform similarly, and in some cases the former outperforms the latter when compared to a full quantum description. The classical mappings are able to capture interference effects, both constructive and destructive, that originate from equivalent energy transfer pathways in the models.

I. INTRODUCTION

The pursuit of classical and semi-classical theories to approximate the quantum dynamics of molecular systems has a long history,^{1–20} and has been motivated by their cost-effectiveness and the fact that chemical dynamics take place often in an energy and density-of-states regime where a classical description can be meaningful. The most wide-spread type of approaches describes the nuclear-electronic non-adiabatic dynamics in molecules by splitting the degrees of freedom into nuclear and electronic subspaces. The nuclei are then set to evolve classically in a potential derived from the interaction with the electrons, while quantum mechanics is maintained for the electronic subspace. The latter dynamics can be described by a time-dependent Schrödinger equation in the discrete space of diabatic or adiabatic electronic states, or by mapping this discrete space into a set of classical variables, which then evolve together with the nuclei under an overall classical Hamiltonian. Several mappings exist for the electronic degrees of freedom, for example the original Meyer-Miller (MM) Hamiltonian consisting of one harmonic oscillator per electronic state, and different flavors of the spin-mapping (SM) Hamiltonian, which use classical spin degrees of freedom to map the state of the electronic subspace^{4,21}. Importantly, Stock and Thoss showed that the nuclear-electronic MM Hamiltonian yields the exact quantum dynamics once re-quantized,¹¹ and this mapping is also known as MMST.

Although the equations of motion (EOM) of mapping approaches are fully classical, this fact is, by itself, not necessarily an approximation. The classical EOM of the MM mapping for the electronic states are formally equivalent to solving the Schrödinger equation they have a close formal resemblance with the Ehrenfest method^{2,4}. The differences are,

however, significant and related to how initial conditions are sampled and to how observables are derived from the trajectories^{2,4,22,23}. One can argue that mapping approaches provide a more fundamental answer to the question of how to mix classical and quantum degrees of freedom than, e.g. Ehrenfest or surface-hopping approaches^{6,7}, and often outperform them in benchmark applications^{18,19,24,25}.

Miller and White took the pioneering step to extend the concept of classical mappings to the treatment of electrons (fermions) under a second-quantized Hamiltonian¹. This step can be motivated by the formal similarity between the second-quantized Hamiltonian for bosons and fermions, and the fact that the bosonic creation/annihilation operators are analogous to the ladder operators of interacting harmonic oscillators, which can subsequently be downgraded to classical variables to obtain a useful mapping. In their work, Miller and White arrived at a mapping for the fermionic operators using the Heisenberg correspondence relation^{26,27} between matrix elements and classical variables. By construction, the Miller-White (MW) mapping respects the sign-change rules of the commutation relations of fermionic operators. Although it is not presented in this way in Ref. 1, this mapping can be alternatively reached by first performing a (exact) Jordan-Wigner transformation of the fermionic Hamiltonian into a corresponding chain of spins²⁸, where so-called sign-change operators $(1 - 2\hat{n}_j)$ appear, and then taking a spin-mapping (SM)^{2–4,23} for each fermionic degree of freedom (cf. Appendix).

In their original work, the MW mapping was not applied to dynamical processes but it was demonstrated that it yields the correct energy for selected electronic configurations of the helium atom and of the hydrogen molecule. Subsequent works reformulated the MW mapping on the basis of a Cartesian Hamiltonian, like in the original MM mapping, while still preserving the sign-change rules of the fermionic operators.^{29–32} This mapping, called Li-Miller mapping (LMM) in a recent publication³², yields the exact dynamics of the fermions in Fock space for non-interacting Hamiltonians²⁹. Based on

^{a)}Electronic mail: ny182@uni-heidelberg.de

^{b)}Electronic mail: sudip.sasmal@pci.uni-heidelberg.de

^{c)}Electronic mail: oriol.vendrell@uni-heidelberg.de

these developments, promising results have been obtained in studies of electronic dynamics and quantum transport in molecular junctions and quantum dots.^{22,23,29–36} These results indicate that a broader range of electronic processes in molecules may be approachable through classical mappings of the electronic degrees of freedom in Fock space, which is one of the motivations for this work.

It turns out that the original MM mapping applied to non-interacting fermionic Hamiltonians, in the same way as the LMM, delivers the exact dynamics of the system when the initial state is a physical fermionic state (cf. Sec. II below). Starting from this observation, in this study we explore this formal connection and examine the applicability of the original MM mapping to the quantum dynamics of electrons in closed systems in a second quantized setting. In section II, the formal connection that explains this equivalence for non-interacting systems is laid down. We proceed by describing the relation between the initial phase space density of the classically mapped system and the initial configuration of the electrons, and propose strategies to sample this phase space density. Section III compares the MM mapping with exact quantum results and with different mappings explicitly designed for fermions, namely the SM with and without inclusion of antisymmetry (the latter corresponds to the original MW mapping), and to the LMM. We compare Hubbard and impurity Hamiltonians, with and without interactions, and consider as well a model for excitonic energy transfer between chromophores. In this model with interactions we show that the classical MM mapping is able to capture interference effects caused by the presence of different energy transfer pathways leading to the same final state, both when the interferences are constructive and destructive. For the model Hamiltonians and parameter ranges considered, we show how the MM mapping performs comparably to the LMM, even outperforming it in some cases, although it uses half the number of classical variables to map the state of the electrons. MM invariably outperforms the SM mapping with (equivalent to MW) and without inclusion of anti-symmetry.

II. THEORY

A. Equation of motion concerning bosons and fermions

The second-quantized Hamiltonian for a many-body system of fermions (electrons in our case) and bosons takes the general form

$$\hat{H} = \hat{H}^{(1)} + \hat{H}^{(2)} \quad (1)$$

$$\hat{H} = \sum_{ij} h_{ij} a_i^\dagger a_j + \frac{1}{2} \sum_{ijkl} V_{ijkl} a_i^\dagger a_j^\dagger a_l a_k, \quad (2)$$

where i, j, k and l run over all single particle states and F is the number of single-particle basis functions used to expand the Fock space. In this paper we will refer to the annihilation (creation) operators as $\hat{a}_j^{(\dagger)}$ in general and specialize them to \hat{b}_j for bosons and \hat{c}_j for fermions whenever this distinction is

needed. These operators obey the respective commutation and (anti-)commutation relations

$$[\hat{b}_i, \hat{b}_j^\dagger] = \delta_{ij}; \quad [\hat{b}_i, \hat{b}_j] = [\hat{b}_i^\dagger, \hat{b}_j^\dagger] = 0; \quad (3)$$

$$\{\hat{c}_i, \hat{c}_j^\dagger\} = \delta_{ij}; \quad \{\hat{c}_i, \hat{c}_j\} = \{\hat{c}_i^\dagger, \hat{c}_j^\dagger\} = 0. \quad (4)$$

As is well known, for bosons one can identify the creation and annihilation operators with the ladder operators of a set of harmonic oscillators, one for each bosonic mode, which obey the same commutation relations. The ladder operators can be expressed using the corresponding positions and momenta

$$\begin{aligned} \hat{b}_j &\mapsto \frac{1}{\sqrt{2}}(i\hat{p}_j + \hat{q}_j) \\ \hat{b}_j^\dagger &\mapsto \frac{1}{\sqrt{2}}(-i\hat{p}_j + \hat{q}_j), \end{aligned} \quad (5)$$

leading to a form of the bosonic Hamiltonian with a simple classical analog. Note that \hbar is set to be 1 which is also applied to all the other equations in below. The equations of motion of the classical positions and momenta follow from the usual prescription: substitute the commutator with the Poisson bracket in the corresponding Heisenberg equations of motion, or equivalently derive Hamilton's equations directly from the classical form of the Hamiltonian. Already Miller and White in their seminal paper recognized that, would fermions obey the same commutation relations as bosons, this analogy would offer a straightforward path towards a classical mapping for fermions¹.

It is useful to first discuss in some detail the properties of a classical approximation to the dynamics of the $\hat{H}^{(1)}$ term for bosons before considering fermions. Using the relations (5) and replacing quantum operators with classical variables one arrives at the Hamiltonian function

$$H_{\text{B;cl}}^{(1)}(\mathbf{p}, \mathbf{q}) = \frac{1}{2} (\mathbf{p}^+ \mathbf{h} \mathbf{p} + \mathbf{q}^+ \mathbf{h} \mathbf{q}) - \gamma \text{Tr}[\mathbf{h}], \quad (6)$$

where the column arrays \mathbf{p} and \mathbf{q} collect all momenta and positions, respectively, and \mathbf{h} is the matrix with elements h_{ij} . The γ factor takes values between 0 and 1/2 and it does not affect the classical equations of motion. However, it determines the amount of zero-point energy available to the classical system when sampling initial conditions^{2,37}. Hence, the results obtained with the mapping for interacting systems depend on γ . In the numerical results discussed below we have made the experience, similarly to other applications in the literature^{22,23}, that $\gamma \approx 0.366$ works best, and this is the value we keep throughout. This Hamiltonian is identical with the electronic part of the original MM Hamiltonian^{2,11,22}, although in this case the classical oscillators do not map the amplitudes of the electronic states, but instead the number of particles in each single particle state, $n_j = (p_j^2 + q_j^2)/2 - \gamma$.

The linear Hamilton's equations arising from Hamiltonian (6) are

$$\dot{\mathbf{q}} = \mathbf{h} \mathbf{p}; \quad -\dot{\mathbf{p}} = \mathbf{h} \mathbf{q} \quad (7)$$

and they are equivalent to the time-dependent Schrödinger equation (TDSE)

$$i\dot{\mathbf{c}} = \mathbf{h} \mathbf{c}, \quad (8)$$

when the complex coefficients $\mathbf{c} = (\mathbf{q} + i\mathbf{p})/\sqrt{2}$ are introduced. This analogy between Hamilton's equations and the TDSE was already recognised by Meyer and Miller in their original work on the MM mapping^{2,22}. However, in the MM case, the coefficients in Eq. (8) are normalized to 1, whereas in the non-interacting bosonic case they are normalized to the number of particles, $P = \mathbf{c}^* \mathbf{c}$. This results in the caveat that unique Fock-space states $|\mathbf{n}\rangle \equiv \{|n_1, \dots, n_F\rangle\}$ do not have a unique parametrization in terms of \mathbf{c} (or \mathbf{q}, \mathbf{p}) because an arbitrary phase can be added to every element of \mathbf{c} without altering $|\mathbf{n}\rangle$, whereby different parametrizations of $|\mathbf{n}\rangle$ lead to different dynamics of the expansion coefficients. This fact is illustrated numerically in some of the examples in Section III. Remacle and Levine had already encountered the non-uniqueness of Eq. (7, 8) to describe a *many-body* system of non-interacting electrons through a *single classical trajectory*, but a workaround was not proposed and only applications to one-electron systems were discussed³⁸.

This caveat can be resolved, still for non-interacting bosons, by considering the time-evolution of the corresponding Wigner density function^{39,40}

$$\dot{\rho}_W(\mathbf{q}, \mathbf{p}) = -2H^{(1)}(\mathbf{q}, \mathbf{p}) \sin\left(\frac{\Lambda}{2}\right) \rho_W(\mathbf{q}, \mathbf{p}), \quad (9)$$

where $\Lambda = \overleftarrow{\nabla}_q \overrightarrow{\nabla}_p - \overleftarrow{\nabla}_p \overrightarrow{\nabla}_q$, and $A_W \Lambda B_W \equiv \{A_W, B_W\}$ indicates the Poisson bracket. Under the quadratic Hamiltonian $H^{(1)}$ only the lowest order expansion of the sine function in Eq. (9) contributes and one immediately arrives at the classical Liouville equation for the density,

$$\dot{\rho}(\mathbf{q}, \mathbf{p}) = \{H^{(1)}(\mathbf{q}, \mathbf{p}), \rho(\mathbf{q}, \mathbf{p})\}, \quad (10)$$

which delivers the *exact* phase-space dynamics of the non-interacting system. This density can be propagated as a swarm of classical trajectories matching the quantum mechanical initial conditions, which is the same as the Wigner classical approximation of Heller⁵. For non-interacting bosons this is not an approximation, but an alternative way to compute the exact dynamics of the system.

Up to now our discussion has been centered on bosonic particles and we have not made progress yet towards our primary goal, the classical mapping of fermionic particles. Let us return to the quantum mechanical problem and consider the time evolution of the single-particle density matrix elements $\langle \hat{a}_j^\dagger \hat{a}_i \rangle$

$$\frac{d}{dt} \langle \hat{a}_j^\dagger \hat{a}_i \rangle = i \left(\sum_k^F h_{kj} \langle \hat{a}_k^\dagger \hat{a}_i \rangle - \sum_l^F h_{il} \langle \hat{a}_j^\dagger \hat{a}_l \rangle \right). \quad (11)$$

Equation (11) is a closed expression: once the F populations $\langle \hat{n}_j \rangle$ and the $F(F-1)$ off-diagonal terms $\langle \hat{a}_j^\dagger \hat{a}_i \rangle$ are specified, their evolution follows uniquely. The key observation is that Eq. (11) is identical for bosons and for fermions. In other words, the same initial one-body density of non-interacting bosonic and fermionic systems has the same time evolution.

The important consequence for our purposes is that the original MM mapping in Eq. (6) also delivers the exact quantum dynamics of non-interacting Hamiltonians for many-body

fermionic systems *once the initial one-body density matrix of the fermionic state has been mapped onto the corresponding phase-space density in Eq. (10)*. This result will be illustrated with various numerical examples below. Note that we have made no attempt to include the anti-symmetry of the fermions through a Jordan-Wigner transformation,²⁸ nor to limit the maximum occupation of the orbitals with a spin mapping (SM) model^{1,23}. As is known²⁹⁻³¹, the mappings based on those concepts do not deliver the *exact* dynamics in the non-interacting limit and, as we will show, they indeed perform poorly compared to the MM mapping, with and without interactions.

The exact dynamics in the non-interacting limit is reproduced as well by the LMM mapping, which is explicitly devised for fermions²⁹⁻³², but at the cost of doubling the size of the classical phase-space compared to the MM mapping. For the range of examples with interactions considered in this work, though, we could not see any significant advantage of the LMM over the MM mapping. It is worth mentioning, however, that the LMM has been developed for, and applied to, semiclassical initial value calculations,²⁹⁻³¹ whereas in this work we consider it in a fully linearized, classical context. For completeness, both the SM and LMM are described in the Appendix.

Finally, two equivalent propagation strategies are available for non-interacting systems: (i) The initial fermionic Fock-space state is mapped onto a corresponding phase-space distribution, Eq. (10), which can then be conveniently discretized as N phase-space trajectories, each evolving as $2F$ coupled Hamilton's equations. (ii) The one-body density matrix corresponding to the initial fermionic state is propagated according to the F^2 coupled differential Eqs. (11). The former strategy is our working approximation for interacting Hamiltonians. The latter strategy, propagating the one-body density matrix, becomes essentially equivalent to solving the full quantum-mechanical problem once interactions are included, and we do not consider approximations along that line.

B. Sampling of initial conditions

Using the relations (5) with the single-particle density matrix elements $\langle \hat{a}_j^\dagger \hat{a}_i \rangle$ and equating expectation values to classical phase-space averages, one can write the relation

$$\begin{aligned} \langle \hat{a}_j^\dagger \hat{a}_j \rangle &= \frac{1}{2} \int (p_j^2 + q_j^2 - 2\gamma) \rho(\mathbf{q}, \mathbf{p}) d^F q d^F p & (12) \\ \langle \hat{a}_j^\dagger \hat{a}_i \rangle &= \frac{1}{2} \int (p_j p_i + q_j q_i - i p_j q_i + i q_j p_i) \rho(\mathbf{q}, \mathbf{p}) d^F q d^F p \end{aligned}$$

between the quantum mechanical matrix element of the one-body density and the classical phase-space average of position and momenta for the MM mapping. The phase-space density can be represented by a discrete set of N phase-space points

$(\mathbf{p}^{(k)}, \mathbf{q}^{(k)})$,

$$\langle \hat{a}_j^\dagger \hat{a}_j \rangle = \frac{1}{N} \sum_{k=1}^N \frac{1}{2} (p_j^{(k)2} + q_j^{(k)2} - 2\gamma) \quad (13)$$

$$\langle \hat{a}_j^\dagger \hat{a}_i \rangle = \frac{1}{N} \sum_{k=1}^N \frac{1}{2} (p_j^{(k)} p_i^{(k)} + q_j^{(k)} q_i^{(k)} - i p_j^{(k)} q_i^{(k)} + i q_j^{(k)} p_i^{(k)}).$$

It is more convenient to discuss the sampling of initial conditions in terms of the corresponding action-angle variables,^{2,37} whose relation to (q_j, p_j) follows compactly as

$$q_j + i p_j = \sqrt{2(n_j + \gamma)} e^{i\phi_j}. \quad (14)$$

Using Eq. (14), Relation (13) becomes

$$\langle \hat{a}_j^\dagger \hat{a}_j \rangle = \frac{1}{N} \sum_{k=1}^N n_j^{(k)} \quad (15a)$$

$$\langle \hat{a}_j^\dagger \hat{a}_i \rangle = \frac{1}{N} \sum_{k=1}^N \sqrt{(n_j^{(k)} + \gamma)(n_i^{(k)} + \gamma)} e^{i(\phi_i^{(k)} - \phi_j^{(k)})}. \quad (15b)$$

Let us consider first the simple case that the initial state in Fock space corresponds to a single configuration with one single electron, $|j\rangle \equiv |0_1, \dots, 1_j, \dots, 0_F\rangle$, in the occupation number representation. In this case $\langle \hat{a}_j^\dagger \hat{a}_j \rangle = 1$ and all other matrix elements of the one-body density matrix are zero. Therefore the one-body density matrix can be mapped to a single phase-space point with action variables $n_j = 1$, $n_l = 0$ for $l \neq j$ and all angle variables $\phi_m = 0$. Integrating the corresponding classical trajectory is of course equivalent to solving the corresponding TDSE, Eq. (8). Another illustrative example is the single-electron case where the initial state is a linear superposition of configurations

$$|\Psi\rangle = \sum_{j=1}^F C_j |j\rangle \quad (16)$$

where C_j are complex expansion coefficients and $|j\rangle$ are the single-electron configurations defined above. Now, by setting $\gamma = 0$, Eqs. (15) can be fulfilled simultaneously by a single phase-space point where the action-angle variables are chosen such that $C_j = \sqrt{n_j} e^{i\phi_j}$. This situation is analogous to setting $\gamma = 0$ in the original MM mapping for electronic states, which then reverts to an Ehrenfest model with a single trajectory. If $\gamma \neq 0$, the one-body density of the single-electron state (16) cannot be described, in general, by a single phase-space point according to Eqs. (15).

A more useful case corresponds to a single-configuration many-body state of the form $|1_1, 1_2, \dots, 1_m, 0_l, \dots, 0_F\rangle$, for example a Hartree-Fock approximation of the ground electronic state or an excited state that can be initially well described as a single configuration. For such a state, the one-body density matrix is diagonal with $\langle \hat{a}_j^\dagger \hat{a}_j \rangle = n_j$. Independently of the choice of γ , it is clearly impossible to fulfill, e.g., that

$$\langle \hat{a}_1^\dagger \hat{a}_1 \rangle = \langle \hat{a}_2^\dagger \hat{a}_2 \rangle = 1 \quad (17a)$$

$$\langle \hat{a}_2^\dagger \hat{a}_1 \rangle = 0 \quad (17b)$$

	ϕ_1	ϕ_2	ϕ_3
Trj 1	0	$\pi/4$	$3\pi/4$
Trj 2	0	$3\pi/4$	$\pi/4$
Trj 3	0	$5\pi/4$	$7\pi/4$
Trj 4	0	$7\pi/4$	$5\pi/4$

TABLE I. In a system with 3 DOFs, an instance is presented by solving Equation (13).

with one single phase-space point. One can think of different ways to sample initial conditions that fulfill Eqs. (15), for example by introducing a specific number N of initial phase-space points and then solving Eqs. (15) for all unknown $n_j^{(k)}, \phi_j^{(k)}$ parameters. For instance, it is possible to set all $n_j^{(k)}$ of each k -point equal to the corresponding spin-orbital populations, Eq. (15a), while the remaining angle variables of each k -point must then be determined such that the remaining sum of phases in Eq. (15b) vanishes. This corresponds to determining $F \times N$ unknowns for the corresponding set of $F(F-1)/2$ non-linear equations and it is not clear, *a priori*, what is the smallest number N of phase-space points needed to map a specific density. We have made no attempt to systematically solve Eq. (15b) for the angles of general initial states. We illustrate the concept with a simple example with $F = 3$ spin-orbitals and 2 particles, which will be considered later numerically. Starting with state $|1, 1, 0\rangle$, one needs at least $N = 4$ points (trajectories) to reproduce the corresponding one-body density matrix and one can easily verify that the angles in Table I result in the cancellation of the phase factors in Eq. (15b). Clearly, the choice of angles in Table I is not unique, only the angle differences between each DOF matter.

Alternatively to the discrete sampling just introduced, it is possible to perform a random sampling of the initial angle variables. For single-configuration initial states, where all off-diagonal matrix elements of the one-body density matrix are zero, this is the most straightforward way to determine initial conditions. The disadvantage is that one may end up propagating more classical trajectories than strictly needed. For systems with many single-particle states (orbitals) F , this is however a straightforward way to proceed, as compared to solving Eq. (15b) for some specific discretization N . In Section III A we numerically illustrate how, for non-interacting systems, both a small set of trajectories with initial angles chosen to fulfill Eq. (15b), and a randomly sampled ensemble with a larger number of trajectories, yield the exact one-body dynamics of the system. For interacting Hamiltonians, Eq. (10) is not equivalent to Eq. (9) and therefore the former does not reproduce the exact dynamics of the one-body density. Moreover, different classical phase-space distributions representing the same initial one-body density result in different time evolutions.

Finally, multi-configurational many-body states have, in general, a non-diagonal one-body density matrix that cannot be factorized. Because the off-diagonal elements are not necessarily equal to zero, the random sampling strategy cannot be applied, and one is left with the alternative of solving Eqs. (15) to determine the initial ensemble of phase space points. In this

work we focus instead on single-configuration initial states.

III. RESULTS AND DISCUSSION

In the following, we compare classical mappings with exact quantum calculations in both non-interacting and interacting systems. Except in the discussion of Fig. 3a, where an explicit comparison between discrete and random sampling is made, the initial conditions for all classical mapping calculations and for all benchmarked mappings are generated by random sampling of the angle variables. All quantum calculations are obtained using the multi-configuration time-dependent Hartree (MCTDH) approach^{41–43} in the second-quantization representation (SQR) formulation^{44–46}, which is equally applicable to fermions and bosons. In Section III A, we address several many-body systems without interactions, where the performance of the different mappings and the inclusion of anti-symmetry can be compared and discussed. Subsequently, Section III B concerns with comparisons between classical mappings and exact quantum results for several many-body systems with interactions, ranging from Hubbard-like Hamiltonians to a model for excitonic energy transfer.

A. Non-interacting systems

1. 2- and 3-site systems

First of all, we compare the MM and SM mapping with the exact electron dynamics in 2- and 3-site tight-binding Hamiltonians

$$\hat{H}_{\text{tb}} = \sum_{\langle i,j \rangle} \sum_{\sigma=\alpha,\beta}^F T(\hat{c}_{j,\sigma}^\dagger \hat{c}_{i,\sigma} + \text{h.c.}), \quad (18)$$

where $\langle i,j \rangle$ indicates that the sum runs over nearest neighbors only. A diagram indicating the interactions between the sites is shown in Fig. 1, where orbital interaction terms are marked with a dotted line and are all set to $T = -0.05$ Hartree. For the MM mapping, one simply applies the relations (5) to Hamiltonian (18) to reach the classical Hamiltonian function. For the SM mapping, one can introduce the anti-symmetry of the fermionic quantum-mechanical operators by first transforming the Hamiltonian to an equivalent form based on spin-1/2 degrees of freedom, the so-called Jordan-Wigner transformation⁴⁷ (JWT),

$$\hat{c}_i^\dagger \rightarrow \prod_{k=1}^{i-1} \hat{S}_k \cdot \hat{\sigma}_i^+ \quad (19a)$$

$$\hat{c}_i \rightarrow \prod_{k=1}^{i-1} \hat{S}_k \cdot \hat{\sigma}_i^- \quad (19b)$$

with $S_k = \exp(i\pi\hat{n}_k)$. This transformation is also the key ingredient involved in the description of fermions in second-quantization within the MCTDH method.^{44,46} Here, $\hat{\sigma}_i^\pm$ are spin-1/2 ladder operators and \hat{S}_k are sign-change operators

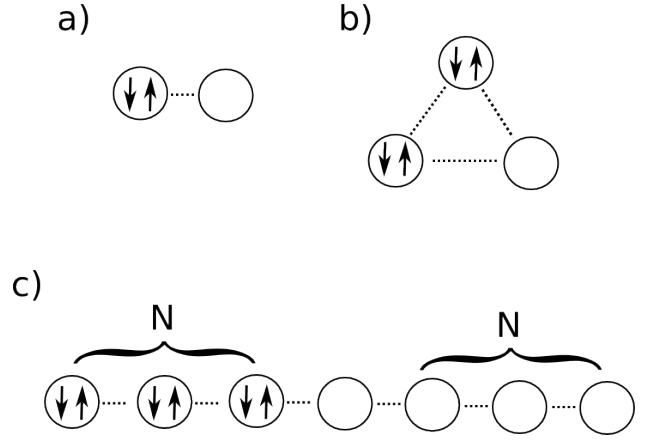


FIG. 1. Structure of a) 2-site and b) 3-site tight-binding systems. The arrows indicate the occupation of the orbitals at $t = 0$ and the dashed lines represent the one-body transfer integrals h_{ij} .

acting locally on index k such that $\hat{S}_k|0_k\rangle = |0_k\rangle$; $\hat{S}_k|1_k\rangle = -|1_k\rangle$, and the spin states are used to indicate occupation: $|\downarrow_k\rangle \rightarrow |0_k\rangle$; $|\uparrow_k\rangle \rightarrow |1_k\rangle$. The sign-change operators can also be written as $\hat{S}_k = 1 - 2\hat{n}_k$, where $\hat{n}_k = \hat{\sigma}_k^+ \hat{\sigma}_k^-$. This substitution together with the JWT relations (19) and the SM result precisely in the original MW mapping for fermionic Hamiltonians (cf. Eqs. 2.10 and 2.13 in Ref. 1).

Applying the JWT to the tight-binding Hamiltonian (18) with linear topology one arrives at a pure spin-1/2 Hamiltonian where all \hat{S}_k operators have cancelled. Therefore, SM and MW (meaning JWT+SM) are equivalent. We examine now the population dynamics of the 2-site tight-binding model starting with site 1 fully populated, Fig. 1a. Since we are dealing with a quantum spin Hamiltonian, one would now be inclined to think that a classical SM representation should deliver a more accurate approximation to the quantum dynamics of the model than MM. We know that this cannot be true because, as already discussed, the MM representation yields the exact dynamics in the non-interacting case. Fig 2 confirms this and also shows how the SM fails to reproduce the exact population dynamics. In fact, the equations of motion of the SM model are not fully linear, which leads to continuous dissipation of the classical trajectories in phase space, and hence to their failure to reproduce the correct amplitude of the population oscillations. This observation is not new, and the reason why Miller and collaborators have developed the LMM Cartesian (oscillator-based) version of the original MW mapping in recent years^{29–32}.

Matters turn more interesting when considering a 3-site tight-binding Hamiltonian with cyclic topology, where the initial occupation of the sites is shown in Fig. 1b. Now, the sign-change operator \hat{S}_2 survives in the term proportional to h_{13} , meaning that the SM and SM+JWT mappings result in different classical Hamiltonians. As expected from our theoretical considerations, the MM mapping reproduces the exact population dynamics, even if now the JWT yields a sign-change operator. The same is found to be true for the LMM (cf. Fig. 3a), which explicitly considers the anti-commutation

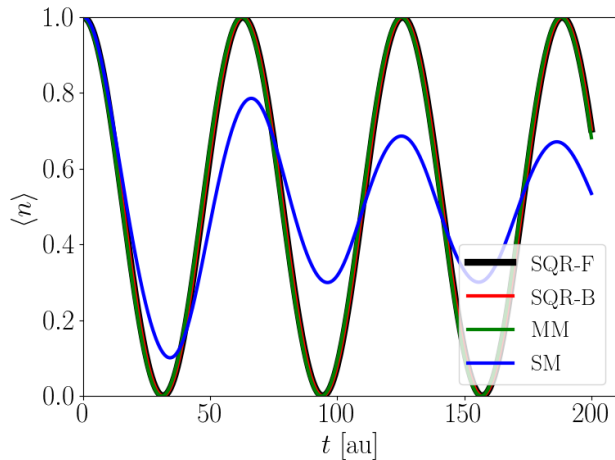


FIG. 2. Time-dependent population of site 1, $n_{1\alpha}$, in the 2-sites tight-binding system for exact fermionic and bosonic dynamics, and for the MM and SM mapping approaches. The transfer integral is set to $T = -0.05$ Hartree.

relations of the fermionic operators. The SM+JWT mapping, instead, again fails to represent the correct site-population dynamics, now even more dramatically than before.

For comparison, we also examine the dynamics of the same 3-site Hamiltonian (6 DOFs) but now the initial one-body density matrix is mapped to $N = 8$ trajectories. The population dynamics in Fig. 3b are seen to be exact for the MM mapping and LMM, whereas they fail to reproduce the quantum result for both the SM and SM+JWT mappings. The two SM-based mappings yield different results when compared among themselves and the SM mapping follows more closely the oscillations of the quantum mechanical population dynamics. From this observation we obtain a first hint at the fact that, including antisymmetry with a JWT before the performing the classical mapping, which is implicit in the MW and LMM treatments^{1,32}, may not actually be relevant to the mapping of fermions and may indeed be counterproductive, resulting in a classical Hamiltonian with higher-order interactions than simpler mappings and a more chaotic classical dynamics that deviates earlier from the correct quantum result. Comparing the random and discrete sampling results of SM-based mappings in Figs. 3a and 3b, we also notice that the discrete mapping based on $N = 8$ trajectories leads to a better description of the oscillations of the populations than the random-sampling results, since fewer trajectories hinder dissipation (through averaging) in the classical phase-space.

Finally, we want to examine the population dynamics in the 3-site system from the perspective of the *individual* trajectories in the random-sampling case. The population of site 1 for each of the 1000 trajectories can clearly grow above $n_1 = 1$ both for the LMM and MM mappings as seen in Fig. 4. Nonetheless these trajectories reproduce in average the exact population dynamics. The common wisdom is that fermionic mappings need to limit by construction the maximum value of the classical action variables at the trajectory level because there can be no more than one fermion per spin-orbital. We

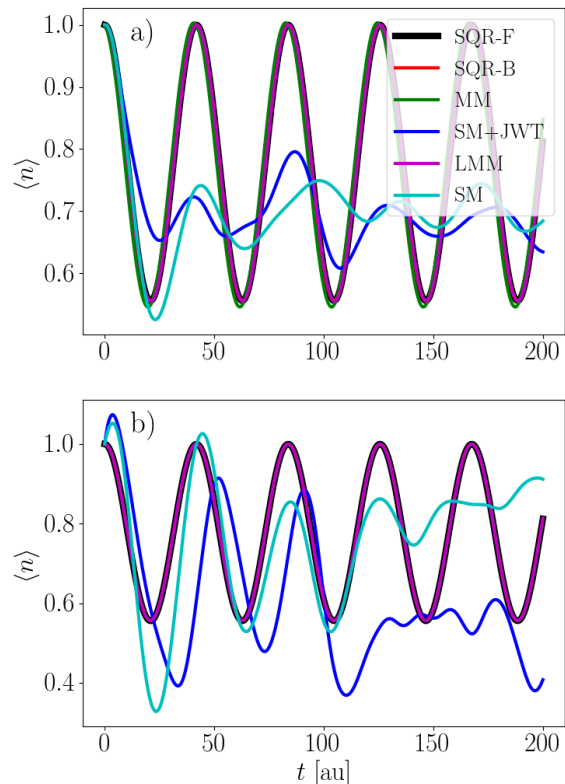


FIG. 3. Time-dependent population of site 1, $n_{1\alpha}$, in the 3-sites cyclic tight-binding system for exact fermionic and bosonic dynamics, and for the MM, SM, SM+JWT and LMM mapping approaches. (a) initial conditions generated by homogeneous random sampling. (b) discrete sampling initial conditions with $N = 8$ trajectories. In both cases all approaches yield the exact result, except the SM and SM+JWT ones.

see, however, that imposing this restriction at the level of individual trajectories is not required for many-body systems without interactions, as only the average value from all trajectories can be given a physical meaning. Even the fermion-tailored LMM can reach populations larger than 1 (cf. Fig. 4b) and still yield the exact averaged population dynamics.

B. Interacting systems

In the previous section, we have discussed why the MM mapping reproduces the exact electron dynamics in non-interaction systems, whenever the initial phase space distribution matches the initial one-body density of the system. Next, we benchmark the performance of the MM mapping in interacting systems against other mappings, and against exact quantum dynamical results. We consider first the Hubbard Hamiltonian, which consists of a tight-binding Hamil-

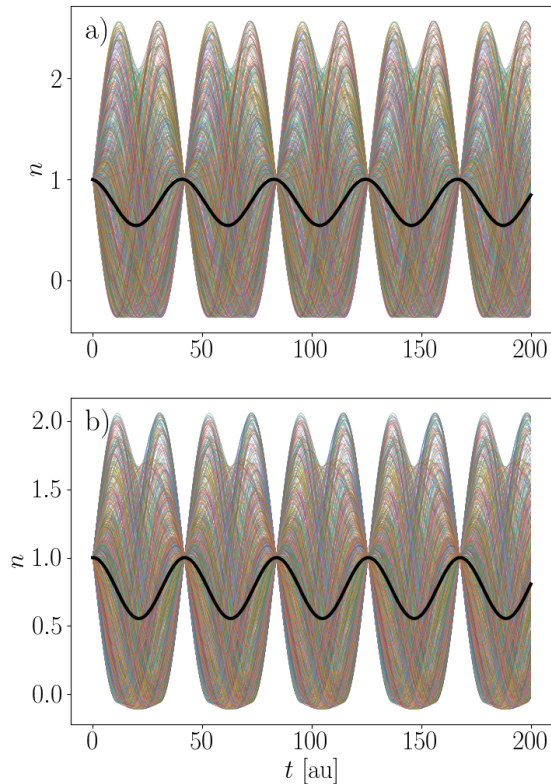


FIG. 4. Time-dependent population of site 1, $n_{1\alpha}$, for each single trajectory in the 3-sites cyclic tight-binding system for a) the MM model and b) the LMM model. Both sets of trajectories yield the same exact expectation value of the population for this non-interacting Hamiltonian. The expectation value $\langle n_{1\alpha} \rangle$ over the trajectories is shown as a thick black line.

tonian plus an on-site repulsion $U\hat{c}_{i,\alpha}^\dagger\hat{c}_{i,\beta}\hat{c}_{i,\alpha}^\dagger\hat{c}_{i,\beta}$. The classical mapping for the Hubbard interaction term takes the form $Un_{i\alpha}n_{i\beta}$, where $n_{i\sigma}$ are functions of the classical phase-space variables. We first consider a cyclic chain with on-site repulsion terms followed by the simulation of different impurity Hamiltonians. Afterwards, we compare the mappings in their ability to describe excitonic energy transfer between model chromophores.

1. 3-site cyclic system

Figure 5a shows the time evolution of the $n_{1\alpha}$ population in the 3-site cyclic system for the ratio $|U/T| = 1$ between the transfer integral and the on-site repulsion. The initial state is the same as for the bosonic and fermionic exact dynamics (cf. Fig 1b) and their population dynamics remains practically identical for more than one period of oscillation. Naturally, fermionic and bosonic population dynamics diverge as time

progresses and follow a completely different time-evolution already after about two periods of oscillation. Both the MM and LMM mappings capture the period of the first oscillation, and the MM mapping follows more closely the trace of both exact fermions and bosons. Incidentally, the MM mapping follows more closely the fermionic than the bosonic population, whereas the LMM mapping is closer to the bosonic than to the fermionic trace after a few oscillations. These results constrained to this particular system and parameters and they should not be overinterpreted. However, they provide two important indications that we are going to explore with further numerical examples: i) The MM mapping, which one could consider as the genuine mapping for bosons, does not necessarily reproduce the bosonic dynamics better than the fermionic one. ii) The LMM, which is devised to reproduce certain aspects of fermionic systems, can indeed in some instances yield results closer to the bosonic time evolution and does not necessarily reproduce the fermionic dynamics more accurately than the simpler MM prescription.

We have seen how, in the absence of interactions, *any* set of trajectories that exactly maps the initial one-body density of the quantum system yields the exact evolution of the populations and one-body correlations. For interacting systems this is not the case anymore. Different initial ensembles encode different two-body densities, and these evolve differently under interactions. The population dynamics in Fig. 5b corresponds to the same parameters as in Fig. 5a but now the initial density one-body density is mapped with only $N = 8$ trajectories, instead of a uniform sampling. Both MM and LMM mappings are found to perform worse in comparison with the quantum mechanical results than the uniform sampling results. However, compared to the uniform sampling, the ensemble dynamics of the discrete sampling retains oscillations for a longer time because a smaller number of phase-space points are being averaged. This indicates that a possible strategy to improve on these results might involve mapping both the one- and two-body densities of the quantum system to the smallest possible number of trajectories, but we are not pursuing this strategy here and instead use the uniform sampling strategy in the following.

In the strong repulsion limit, $U \gg T$ the fermionic and bosonic exact quantum dynamics in Fig 5c quickly diverge. It is surprising that both MM and LMM mappings still reproduce the fermionic dynamics rather well at early times, and we have not been able to develop an intuitive explanation for this fact. An extreme example consists of a system with all spin-orbitals occupied. Under fermionic statistics, such a system is blocked: all its orbital populations remain equal to 1 at all times. Its bosonic counterpart, though, does not experience this Fermi blockade and its populations can present fluctuations. These fluctuations vanish for a non-interacting system, or in the case that the transfer integrals and on-site repulsions are fully symmetric. Figure 5d shows the populations of the fully-occupied Hubbard system with $|U/T| = 1$ (with $U = 0$ for site 1 only). Whereas the quantum fermionic populations remain constant, the bosonic populations fluctuate and so do the populations calculated with both mappings to within a similar range. Intriguing are the fluctuations of the

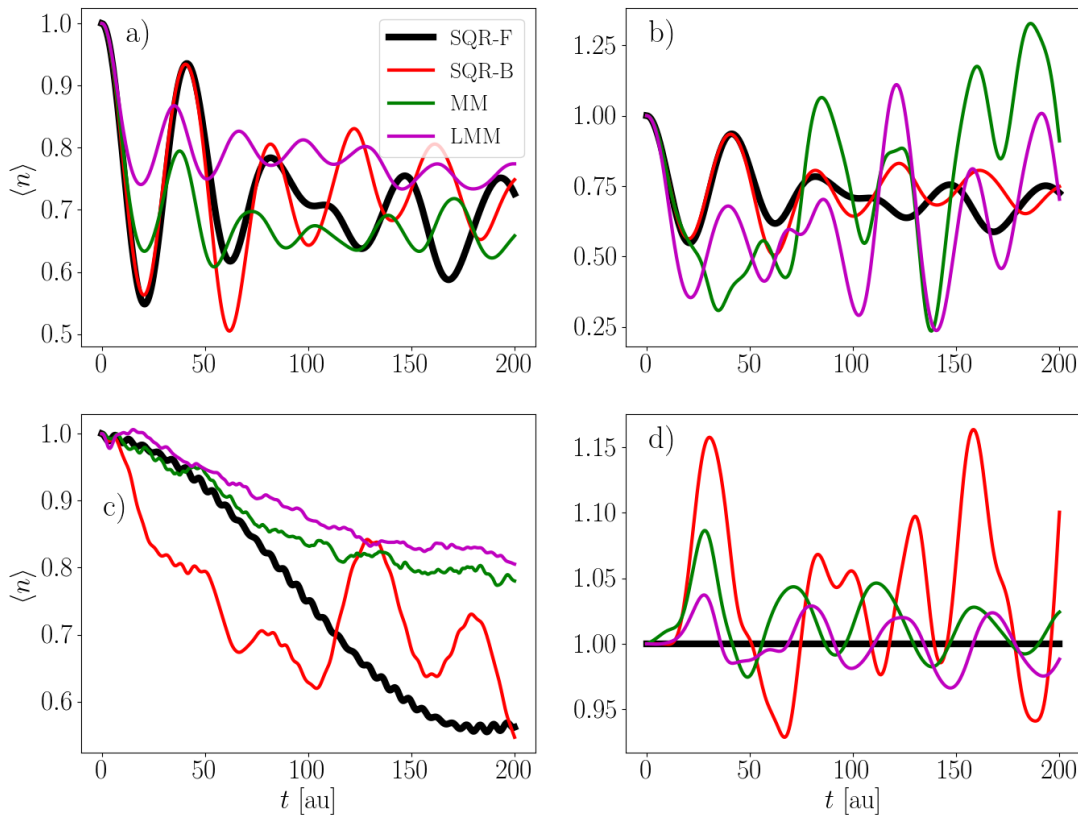


FIG. 5. Population dynamics of $n_{1\alpha}$ for the 3-site cyclic Hubbard model with $T = -0.05$ and $U = 0.05$, except c) where $U = 0.5$. a) uniform sampling; b) discrete sampling; c) strong interaction; d) all spin-orbitals initially populated.

LMM mapping, which is devised to reproduce the behaviour of fermions. This indicates again that the LMM mapping is not superior to the simpler MM prescription at reproducing the dynamics of a fermionic system, and they perform similarly in this connection.

2. Impurity Hamiltonian

Impurity models describe electron transport processes and have been approached by classical mappings in recent works³². Here we consider two tight-binding chains (left and right) of N conduction orbitals coupled to a central single-impurity orbital with a local interaction term U (cf. Fig. 1c). In total each model consists of $2N + 1$ sites and we consider chains with $N = 3, 10$.

Simulations in the $N = 3$ system (7 sites) can still be easily performed quantum mechanically and comparisons with the classical mappings are shown in Fig 6. Simulations with $N = 10$ are only approached using the classical mappings. We consider weak and stronger interaction regimes, $|U/T| = 0.1$ and $|U/T| = 1$, respectively, and set all electrons to be on the

left conduction chain of the impurity model at $t = 0$. These are quite extreme initial conditions in terms of chemical potential if one compares with simulations aimed at reproducing steady-state conditions of the impurity model³². We emphasize that our goal is to benchmark and characterize the performance of the mappings against full quantum results, rather than reproduce specific experimental conditions.

The population (number of electrons) of the left conduction chain and of the central impurity site for the $N = 3$ are shown for the two coupling strengths in Fig 6. The quantum fermionic and bosonic dynamics are similar for both coupling strengths when starting from a fermionic initial state. The exact fermionic calculations require 64 single particle functions (SPF) to span the corresponding sub-Fock spaces of the left and right conduction chains and 4 SPFs for the middle site⁴⁶. The truncated fermionic calculation uses a basis of 40 SPFs for the left and right sites and 4 SPFs for the middle site.

In the case of weak interaction, both the quantum bosonic and fermionic dynamics (red and black traces) remain very similar and both the MM and LMM mappings reproduce the population dynamics extremely well, as seen in Fig 6a and Fig 6c. The worst result corresponds to the non-exact quan-

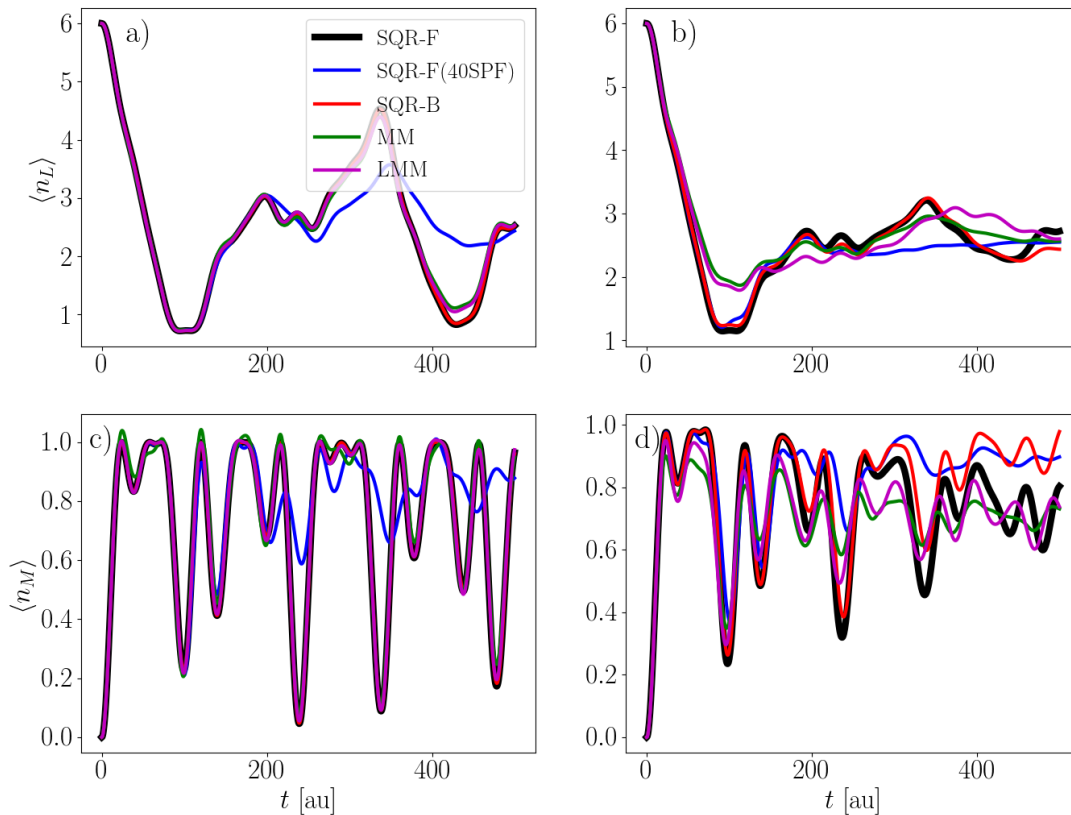


FIG. 6. In a linear chain system ($N = 3$), a) & b) n_L and c) & d) n_M are described. In the system, a) & c) $(T, U) = (-0.05, 0.005)$ while b) & d) $(T, U) = (-0.05, 0.05)$. For all classical mappings, trajectories are generated by the uniform sampling.

tum mechanical calculation with 40 SPFs (blue trace). The reason for this is easily understood. In calculations based on a second-quantization representation^{44,46}, the correlation between the computational degrees of freedom (i.e. the orbital occupations) depends on the hopping integrals T , not on the on-site electron repulsion U . Indeed, the case of stronger electron-electron repulsion is comparatively better described by the approximate quantum calculation as compared to the exact result.

Even in the case of stronger coupling, $|U/T| = 1$, both classical mappings are able to reproduce the population of the conduction chains and impurity site remarkably well (Figs. 6b and 6d). Interestingly, the population of the impurity never surpasses $\langle n_M \rangle = 1$ for either classical mapping even when the electronic flux towards the right conduction chain is maximal during the first 100 au of time. This again strengthens the observation that enforcing a limitation of the maximal population of the fermionic degrees of freedom via the classical mapping (e.g. using classical spin DOFs) is unnecessary, and that the MM performs similarly as LMM while using half the number of classical DOFs.

Finally, we consider an impurity model with $N = 10$ sites in

each conduction chain and show its population dynamics, in Fig 7. where we compare the MM and the LMM mappings for both interaction strengths. As the number of sites increases, the averaged populations of the left, central and right sites becomes more similar between both mappings. The small fluctuations of the central impurity in Figs. 7 are perfectly captured and the population of the impurity does not grow above 1.

C. Excitonic energy transfer

In the previous section, we have shown that the MM mapping can be accurate in systems with weak and medium interactions. Here, we benchmark the applicability of the MM mapping to a second-quantization model for inter-molecular energy transfer between electronically excited molecules mediated by dipole-dipole interactions, i.e. excitonic energy transfer (EET). Although EET has been very successfully described by variational full quantum simulations, for example based on the MCTDH approach⁴⁸, realistic excitonic complexes may consist of many thousands of degrees of freedom, in which case mapping-based approaches might be a useful

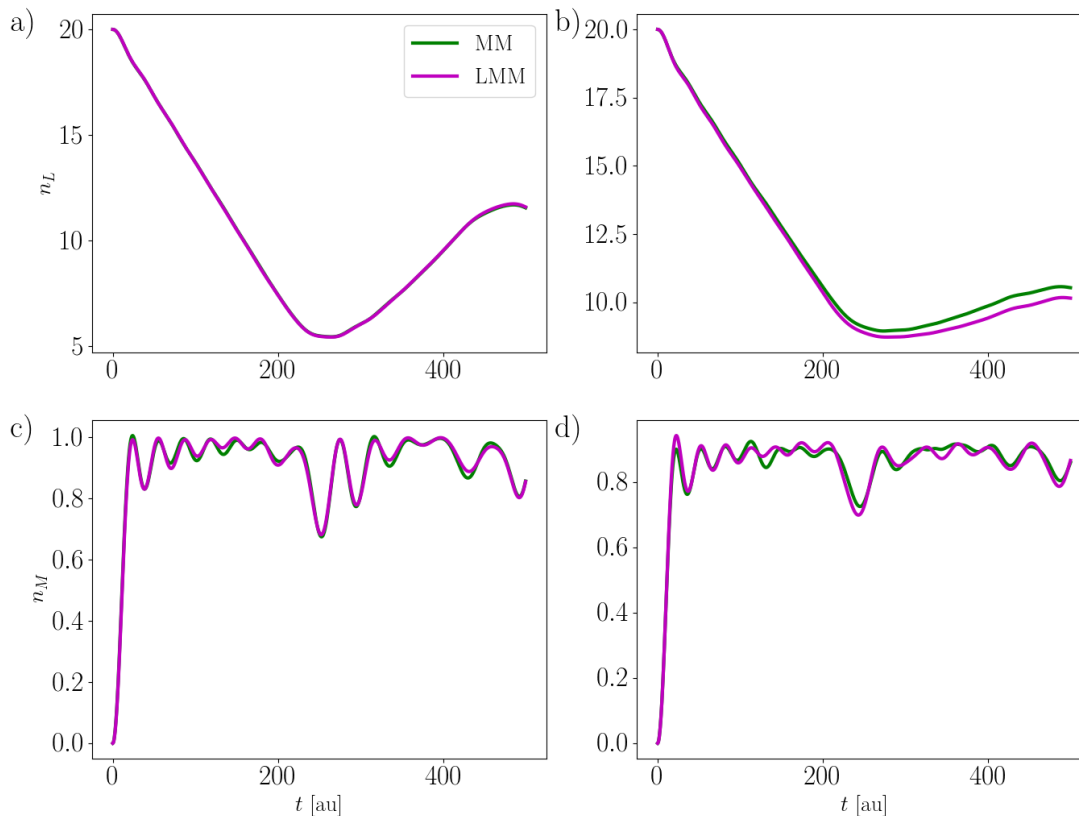


FIG. 7. In a linear chain system ($N = 10$), a) & b) n_L and c) & d) n_M are described. In the system, a) & c) $(T, U) = (-0.05, 0.005)$ while b) & d) $(T, U) = (-0.05, 0.05)$. For all classical mappings, trajectories are generated by uniform sampling.

alternative.

We benchmark the MM and LMM mappings to EET on ethylene clusters (Fig. 8) in various configurations, while keeping the nuclei fixed. Each ethylene molecule is described within an orbital approximation and the construction of the EET model parameters for each cluster proceeds as follows: Localized molecular orbitals are obtained for each ethylene molecule through a separate Hartree-Fock calculation using a minimal atomic basis. Only the highest occupied molecular orbital (HOMO) and lowest occupied molecular orbital (LUMO) in each subsystem are further considered to describe the EET. Hence, each model consists of $4N$ spin-orbitals, where N is the number of ethylene molecules. The electrons are considered independent within each monomer and interact with the electrons of the other monomers via the two-electron Coulomb integrals involving the HOMOs and LUMOs of each monomer pair. Exchange terms are negligible due to distance between the monomers. The one- and two-body electronic integrals for each cluster configuration are provided as supporting information.

We first consider two ethylene molecules facing each other and separated by 10 Å (Fig. 8a). The initial state consists of

one of the molecules singly excited (HOMO→LUMO) and the other molecule in its ground electronic state. The two localized excitonic states are resonant, resulting in a simple periodic EET with a period of about 200 fs. The direct Coulomb repulsion integrals between HOMO and LUMO orbitals in different monomers have values of roughly 1 eV, which contribute to energy shifts of the orbitals. The Coulomb integrals of the form $V_{L_i, H_j}^{L_i, H_j}$ directly drive the exchange of excitation between the monomers and have a value of roughly 50 cm^{-1} . The EET dynamics is approximately captured by the MM and LMM mappings during the first period as seen in Figure (9), where the energy of the acceptor molecule is shown in units of the HOMO-LUMO energy gap. Both mappings fail to capture the full recursions of the exact dynamics due classical phase space dissipation of the ensemble of trajectories. Crucially, however, MM reproduces the initial rate of energy transfer while LMM deviates from the exact curve almost from the onset.

Next, we consider the situation where the EET proceeds through a bridging molecule (Figure (8 b)). The relative orientation between the C-C axis of the donor/acceptor and bridge

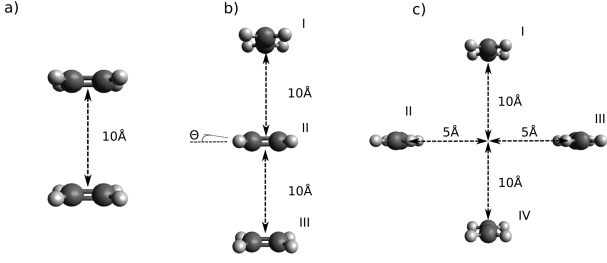


FIG. 8. Ethylene a) dimer, b) trimer, and c) tetramer used in the EET simulations.

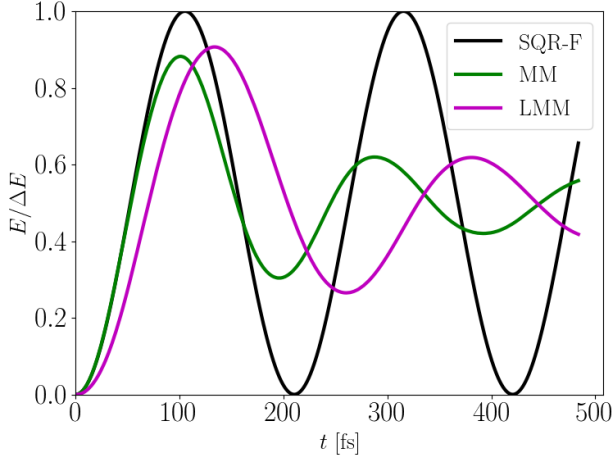


FIG. 9. Energy (in units of the HOMO-LUMO energy gap ΔE) of the acceptor ethylene molecule in the ethylene dimer system.

molecules determines the strength of the dipole-dipole coupling, being it equal to zero for an orthogonal configuration. In the studied cluster, the donor and acceptor systems have a relative orientation of 90 degrees and therefore there is zero energy transfer between them without the intervention of the bridging molecule. A similar system was considered, e.g., in Ref. 49. The bridging system is considered at three angles $\theta = 0, 30, 45$ with respect to the acceptor molecule. For $\theta = 0$, no EET can occur because the transition dipole moments between the donor and the acceptor, as well as the mediator and the acceptor, are zero. For $\theta = 30$ deg., partial EET to the acceptor becomes possible. This partial EET is captured by both the MM and LMM mappings. In both cases, the classical models yield a smaller amount of energy transfer by 10 to 20% with respect to full quantum results after the first half period. As seen in Figs. (a, b), the time-scale of the first period is well captured by the MM mapping, whereas LMM again yields a slower EET dynamics than the exact result. The general trends are similar for $\theta = 45$ degrees. The EET to the acceptor molecule is almost complete after the first half period. Both classical models yield a smaller total energy transfer by about 20% and LMM again yields a slower EET dynamics than the exact result.

Finally, we consider a cluster with four monomers, two act-

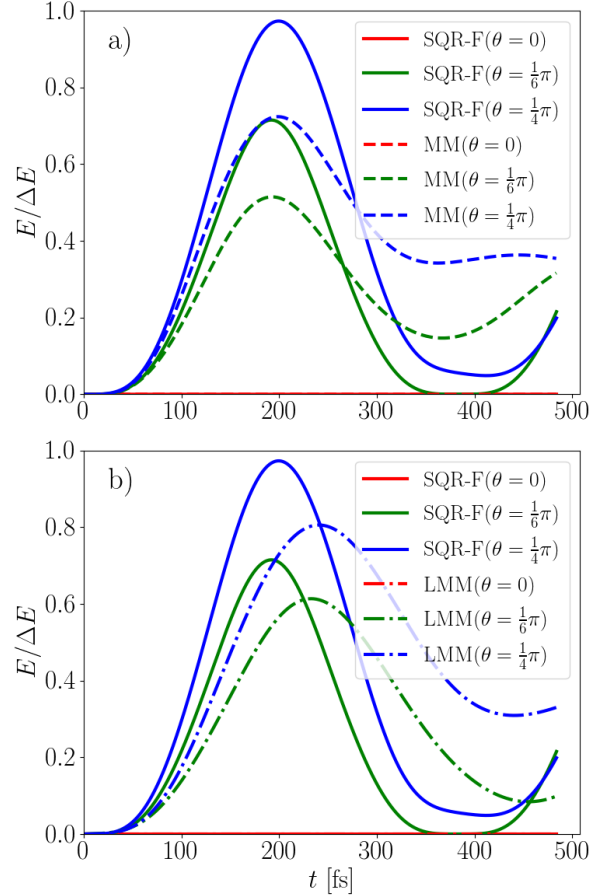


FIG. 10. Energy of the acceptor monomer in the ethylene trimer system (normalized to the HOMO-LUMO energy gap). The donor is initially excited to the first singlet excited state. a) MM mapping and b) LMM mapping compared to the exact quantum mechanical result for different relative orientations of central monomer.

ing as donor (I) and acceptor (IV) systems, while the two other monomers (II, III) act as a symmetrical bridge between the former two. In all cases, monomer I is initially excited at $t = 0$ and the energy of monomer IV as a function of time is shown in Figure (11). The EET is faster when the two bridging pathways constructively interfere. These kinds of coherent EET dynamics involving various pathways are known to operate in models of light-harvesting complexes⁵⁰. The onset of the EET process is well captured by the MM mapping, while the EET described by LMM is slower (cf. slopes during first 100 fs in Figs. (11a) and (11b)). After the first period, about 120 fs, both mappings deviate from the exact result and do not capture the almost complete back-transfer to monomer I after about 270 fs. When one of the pathways is completely suppressed, the EET process also reaches almost 100% yield, although it requires now a longer time, roughly 220 fs, until monomer IV is fully excited. Similarly as before, the initial EET dynamics and the duration of the first half period are captured by the MM mapping. For all the considered ethylene clusters, the MM mapping properly describes the EET rate while the

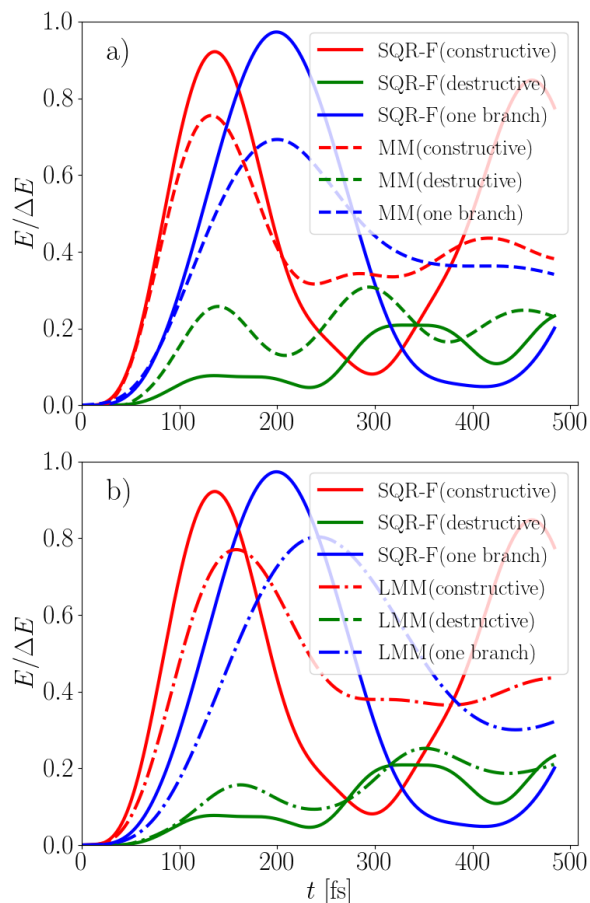


FIG. 11. Energy of the acceptor monomer in the ethylene tetramer system (normalized to the HOMO-LUMO energy gap). The donor is initially excited to the first singlet excited state. a) MM mapping and b) LMM mapping compared to the exact quantum mechanical result.

LMM underestimate the EET rate in the first half period.

Next, we artificially change the sign of the coupling matrix element between monomers II and IV. This results in a destructive interference and the EET process is strongly suppressed, reaching only about 10 to 20% of the EET yield compared to the constructive case. Interestingly, the classical mappings capture this destructive interference effect and describe a strongly suppressed EET process. In this example, LMM reproduces the exact quantum result slightly better than MM at short times, and both mappings describe the EET dynamics approximately to within 10 to 20% of the HOMO-LUMO energy gap for the whole duration of the simulation, about 500 fs.

IV. CONCLUSIONS

We have bench-marked and analyzed the application of various classical mappings (MM, SM, SM+JWT, LMM) to describe the dynamics of fermions (electrons) in Fock space. Our goal has been to establish the range of applicability and

possible drawbacks of the MM mapping and to compare it in detail with the LMM mapping, which includes design principles tailored to the classical description of fermionic dynamics in Fock space.

For non-interacting particles, the MM mapping yields an exact description of the one-body density of the quantum system, provided the dynamics starts from a state with fermionic occupation. This occurs because non-interacting fermionic and bosonic systems starting from identical one-body densities have the same one-body dynamics (cf. Eq. (11)).

Mapping the quantum one-body density to the classical phase space always requires an ensemble of trajectories, the only exception being the case in which only one electron is present. The phase-space mapping can be achieved either by randomly sampling the classical angle coordinates while selecting action-coordinate values that fulfill the initial quantum populations, or by picking a discrete set of points that yield the quantum one-body density when averaged under Eq. (12). Both schemes are equivalent in the non-interacting case.

The SM mapping, with or without a Jordan-Wigner transformation, fails to describe the dynamics of non-interacting systems. This fact was already known and is due to the non-linear nature of Hamilton's equations originating from these models²⁹⁻³¹. Importantly, combining the Jordan-Wigner transformation with the SM, which has been shown to be equivalent to the original MW mapping¹, does not result in any improvement.

We further considered the LMM mapping for fermions in comparison with the simpler MM mapping. LMM uses two vectorial coordinates per fermionic degree of freedom to restrict its maximal occupation and accounts for the sign-rules of fermionic matrix elements through the form of the interacting terms of the classical analog. LMM is in spirit similar to the original MW mapping. It can be obtained by mapping each fermionic DOF to two harmonic oscillators plus including the classical functions of the sign-change operators of a Jordan-Wigner transformation. LMM yields linear equations of motion for the non-interacting case and hence the exact one-body dynamics, but it uses twice as many degrees of freedom as the simpler MM mapping. These two mappings were applied to Hubbard-like cyclic models, to linear-chain impurity models and to models of excitonic energy transfer. Cyclic models provide important insights in the role of anti-symmetry in classical mappings for fermions. This is because the one-body part of the Hamiltonian contains sign-change operators after the JWT, whereas they cancel out in the corresponding linear models. We found that inclusion of these non-linear terms in the MM (and SM) mapping does more harm than good and worsens the description in all considered examples. As mentioned, linear tight-binding and Hubbard Hamiltonians do not feature sign-change operators after the JWT. Hence, the only actual difference between MM and LMM mappings in these examples is the limitation of the maximal orbital occupation in the LMM case. However, this enforced limitation of the LMM mapping plays no particular role in the considered impurity models. The orbital occupation in the central impurity site is very similar in both mappings and always below the maximal occupation of 1 electron

per spin-orbital.

Finally, we considered the process of excitonic energy transfer in model clusters of ethylene. In the models, monomers interact via the two-body integrals calculated from localized Hartree-Fock orbitals in each monomer. We found that the MM mapping correctly captures the initial EET rate (roughly the first half period) and later on deviates from the exact dynamics. LMM leads to a qualitatively similar dynamics compared to MM, although the initial EET rate is often slower than the exact bench-mark result. Both classical mappings correctly capture constructive and destructive interferences resulting from equivalent energy transfer pathways between the donor and acceptor monomers.

Our results indicate that the original MM mapping may be a valid classical analog alternative for the description of fermions in Fock space, and that it does not perform worse than mappings designed specifically for fermions. Our results also cast a question mark on whether the Jordan-Wigner transformation (or an equivalent formulation) is a useful addition to classical mapping strategies for fermions. Our conclusion is that it should be avoided. A limitation by construction of the maximal fermionic occupation does not seem to be necessary either, at least within the bench-marked examples. In fact, in most of the considered examples, the MM mapping outperforms the more complicated LMM. Future work shall consider sampling strategies of the initial phase-space distribution designed for fermions, i.e. explicitly solving Eqs. (15) for a discrete set of phase-space points, as well as the inclusion of nuclear displacements.

SUPPLEMENTARY MATERIAL

See the supplementary material for the 1-electron and 2-electron integrals in ethylene clusters.

ACKNOWLEDGMENTS

J.S. acknowledges the International Max-Planck Research School for Quantum Dynamics (IMPRS-QD) for financial support. The authors are grateful to Prof. Dr. H.-D. Meyer for his valuable suggestions during the preparation of the manuscript and for his critical advice.

DATA AVAILABILITY

The data that support the findings of this study are available from the corresponding author upon reasonable request.

APPENDIX

A. Classical mappings for fermions

A major obstacle in the classical description of fermions is the anti-commutation relation of the fermionic creation and

annihilation operators (3). The anti-commutation relation has two main consequences: it limits the maximum of occupation of the fermionic degrees of freedom in the occupation-number representation and it introduces a ± 1 phase to the corresponding matrix elements depending on the occupation pattern or the orbitals. Classical analogs for fermions attempt to include these properties using different strategies. The orbital occupation can be limited through the use of spin or angular momentum degrees of freedom, whereas the phase of the matrix elements can be included via a Jordan-Wigner transformation from fermionic to spin degrees of freedom followed by the introduction of the classical analog. The form of these mappings for non-interacting systems is introduced in the following for comparison with the MM mapping, and the reader is referred to the original references where the derivations and interacting terms are discussed in detail.

1. SM mapping

The SM mapping has already been utilized as a classical analog for electronic degrees of freedom (DOF) for a finite set of electronic states^{2,3,23,51} and for interacting fermions³⁵. One proceeds by first mapping the fermionic creation-annihilation operators to the angular momentum operators for spin 1/2 degrees of freedom

$$\begin{aligned}\hat{c}_i &\mapsto \hat{\sigma}_{i,x} + i\hat{\sigma}_{i,y} \\ \hat{c}_i^\dagger &\mapsto \hat{\sigma}_{i,x} - i\hat{\sigma}_{i,y},\end{aligned}\quad (20)$$

where $\hat{\sigma}_{i,z} = 1/2$ ($\hat{\sigma}_{i,z} = -1/2$) corresponds to the occupied (empty) i -th one-particle state. The classical Hamiltonian function (for non-interacting particles) without JWT reads

$$\begin{aligned}H_{SM}^{(1)}(\sigma_x, \sigma_y, \sigma_z) &= \sum_i h_{ii} \left(\sigma_{z,i} + \frac{1}{2} \right) \\ &+ 2 \sum_{i>j} h_{ij} (\sigma_{x,i} \sigma_{x,j} + \sigma_{y,i} \sigma_{y,j}).\end{aligned}\quad (21)$$

with classical equations of motion²³

$$\frac{d\vec{\sigma}_i}{dt} = \frac{\partial H(\vec{\sigma}_i)}{\partial \vec{\sigma}_i} \times \vec{\sigma}_i \quad (22)$$

$$\vec{\sigma}_i = (\sigma_{x,i}, \sigma_{y,i}, \sigma_{z,i}). \quad (23)$$

On the other hand, the Jordan-Wigner transformation (JWT) exactly maps a fermionic Hamiltonian to a spin-chain Hamiltonian that yields matrix elements with the correct fermionic phase⁴⁷. Thus, it seems reasonable to combine the SM with the JWT, which introduces phase operators $\hat{S}_k = \exp(i\pi \hat{n}_k)$, and then introduce the corresponding classical functions. These can take the form

$$S_k = (1 - 2n_k), \quad (24)$$

where the occupation $n_j(\vec{x})$ depends on the explicit classical variables \vec{x} used in the corresponding mapping. The SM+JWT

classical analog Hamiltonian for non-interacting particles then takes the form

$$H_{\text{SM+JWT}}^{(1)}(S_x, S_y, S_z) = \sum_i h_{ii} \left(S_{z,i} + \frac{1}{2} \right) + 2 \sum_{i>j} \prod_{k=j+1}^{i-1} h_{ij} (1 - 2n_k) (S_{x,i} S_{x,j} + S_{y,i} S_{y,j}). \quad (25)$$

Comparing Eq. (25) with the relation 2.10 in Ref. 1 shows that this procedure is equivalent to the original Miller-White mapping.

2. LMM mapping

The Li-Miller mapping (LMM) uses the concept of quaternion operators to capture the properties of second-quantized fermionic operators and to construct a classical mapping for them^{29–31}. This results in a mapping where each fermionic DOF is mapped to two classical DOFs (two position-momentum pairs). The LMM has been introduced in the context of semi-classical initial-value representation calculations mechanics^{29–31}, whereas here we use it in a fully linearized context. Recent applications of a classical analog to quantum transport of fermions have modified the LMM mapping in a way that makes it possible describe a few extra types of fermionic operator products, and termed it complete quasi-classical map (CQM)³². In our applications, the LMM and CQM maps are equivalent. The corresponding Hamiltonian reads

$$H_{\text{LMM}}^{(1)}(\mathbf{p}_x, \mathbf{q}_x, \mathbf{p}_y, \mathbf{q}_y) = \frac{1}{2} (\mathbf{q}_x^+ \mathbf{h} \mathbf{p}_y - \mathbf{q}_y^+ \mathbf{h} \mathbf{p}_x) + \gamma \text{Tr}[\mathbf{h}]. \quad (26)$$

The corresponding Hamilton equations of motion for a non-interacting Hamiltonian read

$$\begin{aligned} \dot{\mathbf{q}}_x &= -\mathbf{h} \mathbf{q}_y; & \dot{\mathbf{p}}_x &= -\mathbf{h} \mathbf{p}_y \\ \dot{\mathbf{q}}_y &= \mathbf{h} \mathbf{q}_x; & \dot{\mathbf{p}}_y &= \mathbf{h} \mathbf{p}_x. \end{aligned} \quad (27)$$

- ¹W. H. Miller and K. A. White, *J. Chem. Phys.* **84**, 5059 (1986).
²H. D. Meyer and W. H. Miller, *J. Chem. Phys.* **70**, 3214 (1979).
³H. Meyer and W. H. Miller, *J. Chem. Phys.* **71**, 2156 (1979), <https://aip.scitation.org/doi/pdf/10.1063/1.438598>.
⁴H.-D. Meyer and W. H. Miller, *J. Chem. Phys.* **72**, 2272 (1980).
⁵E. J. Heller, *J. Chem. Phys.* **75**, 2923 (1981).
⁶J. Tully, *J. Chem. Phys.* **93**, 1061 (1990).
⁷S. Hammes-Schiffer and J. C. Tully, *J. Chem. Phys.* **101**, 4657 (1994).
⁸C. C. Martens and J.-Y. Fang, *J. Chem. Phys.* **106**, 4918 (1997).
⁹R. Kapral and G. Ciccotti, *J. Chem. Phys.* **110**, 8919 (1999).
¹⁰D. Mac Kernan, G. Ciccotti, and R. Kapral, *J. Phys. Chem. B* **112**, 424 (2008).
¹¹G. Stock and M. Thoss, *Phys. Rev. Lett.* **78**, 578 (1997).
¹²M. Thoss and G. Stock, *Phys. Rev. A* **59**, 64 (1999).
¹³M. Ben-Nun, J. Quenneville, and T. J. Martínez, *J. Phys. Chem. A* **104**, 5161 (2000).
¹⁴B. F. E. Curchod and T. J. Martínez, *Chem. Rev.* **118**, 3305 (2018).
¹⁵I. Tavernelli, *Phys. Rev. A* **87**, 042501 (2013).
¹⁶B. F. E. Curchod, I. Tavernelli, and U. Rothlisberger, *Phys. Chem. Chem. Phys.* **13**, 3231 (2011).
¹⁷F. Agostini, S. K. Min, A. Abedi, and E. K. U. Gross, *J. Chem. Theory Comput.* **12**, 2127 (2016).
¹⁸J. E. Runeson and J. O. Richardson, *J. Chem. Phys.* **151**, 044119 (2019).
¹⁹J. E. Runeson and J. O. Richardson, *J. Chem. Phys.* **152**, 084110 (2020), <https://doi.org/10.1063/1.5143412>.
²⁰H. Lang, O. Vendrell, and P. Hauke, *J. Chem. Phys.* **155**, 024111 (2021).
²¹S. J. Cotton and W. H. Miller, *J. Phys. Chem. A* **119**, 12138 (2015).
²²S. J. Cotton and W. H. Miller, *J. Chem. Phys.* **139**, 234112 (2013).
²³S. J. Cotton and W. H. Miller, *J. Phys. Chem. A* **119**, 12138 (2015).
²⁴R. Liang, S. J. Cotton, R. Binder, R. Hegger, I. Burghardt, and W. H. Miller, *J. Chem. Phys.* **149**, 044101 (2018).
²⁵X. Gao, M. A. C. Saller, Y. Liu, A. Kelly, J. O. Richardson, and E. Geva, *J. Chem. Theory Comput.* **16**, 2883 (2020), pMID: 32227993.
²⁶W. H. Miller, *J. Chem. Phys.* **64**, 2880 (1976).
²⁷W. H. Miller and C. W. McCurdy, *J. Chem. Phys.* **69**, 5163 (1978).
²⁸P. Jordan and E. Wigner, *Zeitschrift für Physik* **47**, 631 (1928).
²⁹B. Li and W. H. Miller, *J. Chem. Phys.* **137**, 154107 (2012).
³⁰B. Li, T. J. Levy, D. W. H. Swenson, E. Rabani, and W. H. Miller, *J. Chem. Phys.* **138**, 104110 (2013).
³¹B. Li, W. H. Miller, T. J. Levy, and E. Rabani, *J. Chem. Phys.* **140**, 204106 (2014).
³²A. Levy, W. Dou, E. Rabani, and D. T. Limmer, *J. Chem. Phys.* **150**, 234112 (2019).
³³J. W. Zwanziger, E. R. Grant, and G. S. Ezra, *J. Chem. Phys.* **85**, 2089 (1986).
³⁴T. Van Voorhis and D. R. Reichman, *J. Chem. Phys.* **120**, 579 (2004).
³⁵D. W. H. Swenson, T. Levy, G. Cohen, E. Rabani, and W. H. Miller, *J. Chem. Phys.* **134**, 164103 (2011).
³⁶J. Liu, *J. Chem. Phys.* **145**, 204105 (2016), <https://doi.org/10.1063/1.4967815>.
³⁷S. J. Cotton and W. H. Miller, *J. Chem. Theory Comput.* **12**, 983 (2016).
³⁸F. Remacle and R. D. Levine, *J. Chem. Phys.* **113**, 4515 (2000).
³⁹D. J. Tannor, *Introduction to quantum mechanics: a time-dependent perspective*, edited by L. A. Young (University Science Books, 2007).
⁴⁰K. İmre, E. Özizmir, M. Rosenbaum, and P. F. Zweifel, *J. Math. Phys.* **8**, 1097 (1967).
⁴¹H.-D. Meyer, U. Manthe, and L. Cederbaum, *Chem. Phys. Lett.* **165**, 73 (1990).
⁴²M. H. Beck, A. Jäckle, G. A. Worth, and H.-D. Meyer, *Phys. Rep.* **324**, 1 (2000).
⁴³G. A. Worth, M. H. Beck, A. Jäckle, O. Vendrell, and H.-D. Meyer, The MCTDH Package, Version 8.2, (2000). H.-D. Meyer, Version 8.3 (2002), Version 8.4 (2007). O. Vendrell and H.-D. Meyer Version 8.5 (2013). Version 8.5 contains the ML-MCTDH algorithm. Current versions: 8.4.18 and 8.5.11 (2019). See <http://mctdh.uni-hd.de/>.
⁴⁴H. Wang and M. Thoss, *J. Chem. Phys.* **131**, 024114 (2009).
⁴⁵U. Manthe and T. Weike, *J. Chem. Phys.* **146**, 064117 (2017).
⁴⁶S. Sasmal and O. Vendrell, *J. Chem. Phys.* **153**, 154110 (2020).
⁴⁷P. Jordan and E. P. Wigner, “Über das paulische äquivalenzverbot,” in *The Collected Works of Eugene Paul Wigner: Part A: The Scientific Papers*, edited by A. S. Wightman (Springer Berlin Heidelberg, 1993) pp. 109–129.
⁴⁸H. Tamura, M. Huix-Rotllant, I. Burghardt, Y. Olivier, and D. Beljonne, *Phys. Rev. Lett.* **115**, 107401 (2015).
⁴⁹J. S. Ford and D. L. Andrews, *Chem. Phys. Lett.* **591**, 88 (2014).
⁵⁰S. Tomasi and I. Kassal, *J. Phys. Chem. Lett.* **11**, 2348 (2020).
⁵¹H. Meyer and W. H. Miller, *J. Chem. Phys.* **72**, 2272 (1980), <https://doi.org/10.1063/1.439462>.